Solid Earth
Discussions
Open Access
EGU

Structural Disorder of Graphite and Implications for Graphite Thermometry

Martina Kirilova[1], Virginia Toy[1], Jeremy S. Rooney[2], Carolina Giorgetti[3], Keith C. Gordon[2], Cristiano Collettini[3]

[1] Department of Geology, University of Otago, PO Box 56, Dunedin 9054, New Zealand

[2] Department of Chemistry, University of Otago, PO Box 56, Dunedin 9054, New Zealand

[3] Dipartimento di Scienze della Terra, Università degli Studi La Sapienza, Rome, Italy

Correspondence to: Martina Kirilova (martina.a.kirilova@gmail.com)

Key Points:

- graphite, disorder, thermometry, Raman

Abstract

Graphitization, or the progressive maturation of carbonaceous material, is considered an irreversible process. Thus, the degree of graphite crystallinity has been calibrated as an indicator of the peak metamorphic temperatures experienced by the host rocks. However, discrepancies between temperatures indicated by graphite crystallinity versus other thermometers have been documented in deformed rocks. To examine the possibility of mechanical modifications of graphite structure and the potential impacts on graphite 'thermometry' we performed laboratory deformation experiments. We sheared highly crystalline graphite powder at normal stresses of 5 and 25 MPa and aseismic slow sliding velocities of 1 µm/s, 10 µm/s and 100 µm/s. The degree of graphite crystallinity both in the starting and resulting materials was analyzed by Raman microspectroscopy. Our results demonstrate consistent decrease of graphite crystallinity with increasing shear strain. We conclude that the calibrated graphite 'thermometer' is ambiguous in active tectonic settings and we suggest that a calibration that accounts for shear strain is needed.

1 Introduction

Organic matter, preserved in sedimentary rocks, can be transformed into crystalline graphite due to structural and compositional changes during diagenesis and metamorphism, a process known as graphitization (Beyssac et al., 2002a; Bonijoly et al., 1982; Buseck and Beyssac, 2014; Wopenka and Pasteris, 1993; etc.). Graphitization is thought to be an irreversible process and graphite is known to remain stable to the highest temperatures of granulite facies and the highest pressures of coesite-eclogite facies (Buseck and Beyssac, 2014). It is generally accepted that the degree of graphite crystallinity, or its structural order, is determined mainly by the maximum temperature conditions experienced by the host rocks, whereas lithostatic pressure and shear strain are considered to have only minor influence on graphitization (Bonijoly et al., 1982; Wopenka and Pasteris, 1993; Bustin et al, 1995). Therefore, graphite crystallinity has been calibrated as an indicator of the peak temperatures reached during progressive metamorphism (Beyssac et al., 2002a; Reitmeijer and McKinnon, 1985). However, in strained rocks discrepancies between temperatures indicated by the crystallinity of graphite vs. other thermometers have been reported (Barzoi, 2015; Nakamura et al., 2015; Kirilova et al., in review). Thus, numerous authors have speculated that tectonic deformation results in graphite structural modifications that challenge the validity of the existing graphite thermometers (Large et al., 1994; Bustin et al, 1995; Crespo et al., 2006; Barzoi, 2015; Nakamura et al., 2015).

Furthermore, graphite occurrence and enrichment have been documented in several fault zones in the world, e. g. the Alpine Fault zone, New Zealand (Kirilova, et al., in review), the Hidaka metamorphic belt, Hokkaido, Japan (Nakamura et al., 2015), the Atotsugawa fault system, Japan (Oohashi, et al., 2012), the Tanakura Tectonic Line, Japan (Oohashi et al., 2011), the Err nappe detachment fault, Switzerland (Manatschal, 1999), and the KTB borehole, Germany (Zulauf et al., 1990). In these intensely deformed rocks its presence is of particular interest because its low friction at $\mu \sim 0.1$ (Morrow et al., 2000) allows graphite to act as a natural solid lubricant (Savage, 1948). The mechanical behavior of graphite has been broadly investigated in both natural and experimental specimens, where it manifests with the lowest μ among sheet structure minerals (Moore and Lockner, 2004; Oohashi et al., 2011, 2013; Rutter, et al., 2013; Kuo et al., 2014, etc.) confirming it could have a significant impact on fault mechanics. It has been experimentally proven that even a small fraction of graphite has disproportionally large effect on frictional strength due to concentration of smeared graphite layers (Rutter, et al., 2013).

However, structural changes in crystalline graphite caused by tectonic deformation have not been explained until now. To examine this aspect and to investigate the potential impacts of structural disordering of graphite on the graphite 'thermometer', we have carried out laboratory deformation experiments on highly crystalline graphite powder.

2 2 Experimental methods

2.1 Sample description

As a starting material in the current study we used synthetic (or commercially synthesized) graphitic carbon to avoid complexities arising from variable degree of crystallinity in natural carbon materials. Initially, the material was crushed to 160 µm in a RockLabs Swing (TEMA) mill. The resulting fine graphitic powder was 'cooked' at 700˚C for two hours in a Lindberg Blue M Muffle Furnace to achieve full graphitization, which is known to occur at this temperature in the absence of other variations in physical conditions (Buseck and Beyssac, 2014). This was used as the starting material for the deformation experiments.

2.2 Experimental procedure

In total, 10 deformation experiments were performed at room temperature and room humidity in the Brittle Rock Deformation Versatile Apparatus BRAVA (Collettini et al., 2014), at INGV, Rome. For each experiment two 3-mm thick layers of synthetic graphite gouges were placed in between three grooved forcing blocks in a double-direct shear configuration (e.g. Dieterich, 1972). The two side blocks are held stationary, and the central forcing block is driven downward causing shear to occur within the graphite gouge layers. Normal stress is applied by the horizontal piston in load-feedback control mode and shear displacement accomplished by the vertical piston in displacement-feedback control mode. Forces are measured with stainless steel load cells ($\pm$ 0.03 kN) and displacements are measured with LVDTs ($\pm$ 0.1 µm) attached to each piston. Experiments have been conducted at normal stresses of 5 MPa or 25 MPa and aseismic sliding velocities of 1 µm/s, 10 µm/s and 100 µm/s. The experiments were carried out to total displacements of 20 mm. In addition, some experiments were stopped at 5 mm and 10 mm and the specimens were then recovered to reveal graphite structural changes that took place during different amounts of total deformation. The coefficient of friction (μ) was calculated as the ratio of measured shear load to measured normal load ($\mu = \tau / \sigma_n$, where τ is shear stress and σ_n is effective normal stress). The average shear strain (γ) within the layer was calculated by dividing shear displacement increments by the measured layer thickness and summing. The displacement values of the vertical and horizontal load points were corrected for the elastic stretch of each load frame, taking into account that the machine stiffness is 1283 kN/mm on the horizontal axis and 928.5 kN/mm on the vertical axis.

2.3 Raman microspectroscopy

The degree of graphite crystallinity was measured by an Alpha 300R+ confocal Raman microscope (WITec, Ulm, Germany) with a 532 nm laser (Coherent, Santa Clara, California), located at the Department of Chemistry, University of Otago, New Zealand. The laser (3.0 mW) was focused on the samples with a 50× Zeiss objective. The scattered light was dispersed with

79   a 1200 g/mm grating. The combination of the 50× objective and 532 nm laser wavelength produced a laser spot size of

80   approximately 412 nm in diameter. The integration time of each spectrum was 2 seconds with 50 co-additions (100 seconds

81   in total). The spectra were calibrated using the Raman band from a silicon wafer prior to each set of measurements.

82   The collected spectra were pre-processed in GRAMS AI 9.1 (Thermo Fisher Scientific Inc.), where cosmic spikes were

83   removed and a multi-point linear baseline offset was performed. This was followed by peak fitting three Lorentzian-

84   Gaussian functions to each spectrum with a linear baseline over 1000 - 1700 cm^{-1}. For each spectrum, the area ratio was

85   calculated (R2 = AD1 / (AG + AD1 +AD2), where Ai = area of the ith peak) (Beyssac et al.., 2002a; Wopenka and Pasteris,

86   1993).

87   **2.4 Scanning electron microscopy**

88   Microstructural analyses of the graphite gouge recovered from the biaxial apparatus were carried out using a scanning

89   electron microscope (SEM). Some SEM images were acquired from the shiny surfaces of the graphite layers that had been

90   parallel to the center and or side forcing blocks (Y-Z sections), with a Zeiss Sigma field emission scanning electron

91   microscope (VP FEG SEM) at the Otago Centre for Electron Microscopy (OCEM), University of Otago, New Zealand. The

92   instrument was operated in variable pressure mode (VP) at 15 kV using a working distance (WD) of 7 – 8 mm and a VPSE

93   (VP-mode secondary electrons) detector. In addition, polished thin sections cut perpendicular to the surface of contact with

94   the center and side forcing blocks (X-Z sections) were imaged on a JEOL JSM-6510 SEM at the University of Potsdam,

95   Germany, where high-resolution secondary electron images were collected at 20 kV and a WD of 10 mm.

96   **3 Results**

97   **3.1 Mechanical data**

98   Our experiments allowed us to investigate graphite mechanical behavior and structural modifications under various sliding

99   velocities, normal stresses and shear strain. These conditions are summarized in Table 1.

100   **3.1.2 Friction variations**

101   Over several mm of displacement, the friction coefficient shows a similar evolution trend in all experiments. On a plot of

102   friction vs. displacement (Fig. 1a), the friction coefficient (μ) delineates a curve characterized by a rapid increase to an initial

103   peak friction (μ_{peak}), followed by a subsequent exponential decay towards a steady-state friction (μ_{ss}) over a slip weakening

104   distance. The shapes of the friction-displacement curves vary with the normal stress applied and are steeper for the

105   experiments conducted at 25 MPa than the ones at 5 MPa (Fig. 1a) i.e. the displacement required to achieve steady-state

106   decreases at higher normal stress. In addition, the values of both μ_{peak} and μ_{ss} (Fig. 1a; Table 1) are significantly lower in the

107   experiments at 25 MPa (μ_{peak} = ~0.4; μ_{ss} = ~ 0.1) than in the experiments at 5 MPa (μ_{peak} = ~0.5; μ_{ss} = ~ 0.2). Plots of μ at all

108   slip rates (Fig. 1a) indicate a gradual decrease of μ_{peak} with increasing shear velocity at high normal stress (Table 1). In the

109   experiments at 5 MPa subtle variations in μ_{peak} also occur but a velocity-related trend is not observed. μ_{ss} does not depend in

110   any experiment on slip rates, and μ_{ss} remains constant for experiments at both low and high normal stress (Fig. 1a; Table 1).

3.1.3 Shear strain variations

112   Plots of friction vs. shear strain (Fig. 1b) show significant variations in shear strain (γ) attained over equivalent sliding

113   displacements. The estimated shear strain values are a geometric consequence of different thickness changes. Consideration

114   of the shear strain at equivalent sliding velocities but different normal stresses demonstrates that shear strains achieved

115   during the 5 MPa experiments are approximately half of those at 25 MPa (Fig. 1b; Table 1). In addition, the experiments at

116   25 MPa demonstrate a dramatic increase in shear strain with increasing slip velocity (Fig. 1b; Table 1), whereas at low

117   normal stress we do not observe any systematic variations associated with changes in sliding velocities (Fig. 1b, c and d).

118   Fig. 1c and d show the experiments at low shear strain used to characterize graphite structural changes in the early stages of

119   deformation (Table 1).

3.2 Graphite crystallinity

121   All the experiments resulted in the development of shiny smooth surfaces with gentle slickenlines (macroscopic fine

122   grooves, parallel to the slip direction as defined by Toy et al., in press). Raman spectra obtained on the top of these surfaces,

123   that had accommodated most of the induced deformation, are compared to Raman spectra from the starting material to

124   identify the effects of mechanical deformation on graphite crystallinity.

125   Raman data from 20 spectra per sample are presented in Supplementary material 1 (S1). Representative spectra for each

126   sample are illustrated in Fig. 2, which shows spectra displaying the least (left column) and the most (right column)

127   disordered graphite within a sample (i. e. lowest and highest R2 values respectively). Spectra that were typical of the average

128   for each sample are also presented (middle column). Experiments 3 and 7 were stopped at only 5 mm displacement and

129   resulted in extremely fragile deformed surfaces, which were unable to be extracted without them breaking into pieces too

130   small to obtain spectra from. Thus, graphite crystallinity was not measured in these experiments.

131   All the acquired spectra show typical G, D1 and D2 bands, respectively at ~1580 cm^{-1}, ~1350 cm^{-1} and ~1620 cm^{-1} (S1). The

132   degree of graphite crystallinity in each sample could thus be calculated by using the area ratio R2 (Fig. 2; S1). Raman

133   spectra collected from the starting material show R2 values ranging from 0 to 0.327 (Fig. 2), corresponding respectively to

134   fully crystalline and highly organized graphite. Spectra acquired from the deformed surfaces show higher R2 values (Fig. 2;

135   S1). The most crystalline graphite with R2=0.330 was produced in Exp. 2 (Fig. 2) while the most disordered graphite with

136   R2=0.661 resulted from Exp. 10 (Fig. 2).

137 As graphite crystallinity vary within a sample (Fig. 2; S1), we examine average R2 values for each one and compare them

138 with applied normal stress, sliding velocity and shear strain (Table 2). The starting material has average $R2_{\text{pre-shear graphite}}$ =

139 0.173, whereas all deformed samples have higher average R2 values (Table 2). Analyzing the average R2 values for

140 deformed samples reveals that graphite is more disordered in the high-pressure experiments (Table 2) than in the

141 experiments at 5 MPa. Furthermore, in the experiments at 25 MPa the average graphite crystallinity decreases with

142 increasing sliding velocities (Table 2). In contrast, at low normal stress, we do not observe any dependence of the degree of

143 graphite crystallinity on the applied sliding velocities (Table 2). Overall graphite appears as most disordered in the

144 experiments where the highest shear strain was achieved (Table 2). This relationship is illustrated in Fig. 3 by fitting a power

145 function with a correlation coefficient R^2 = 0.96. The experiments 2 and 6 at low normal stress, which were stopped at 10

146 mm displacement and accommodated the least amount of shear strain, contain the least disordered graphite (Fig. 3; Table 2).

147 **3.3 Microstructural characteristics**

148 Similar microstructural features were observed in all the deformed samples. SEM images obtained from the sample

149 deformed during experiment 8 are presented to demonstrate our observations (Fig. 4).

150 These high-resolution images in Y-Z sections reveal that the shiny surfaces are decorated by closely spaced (from < 5 to 10

151 micrometers) slickenlines (Fig. 4a), on top of a smooth continuous layer. In places, the continuity of this layer is interrupted

152 by fine (~1 to 2 micrometers in width) fractures (Fig. 4a), with random orientation compared to the slip direction.

153 Occasionally, the deformed surface appears as completely disrupted, comprising of platy graphite crystals 10 to 50

154 micrometers in size, oriented nearly parallel to the shear direction (Fig. 4b). In X-Z sections this highly deformed surface is

155 observed as a thin slip-localized zone, composed of well-compacted layer of aligned graphite grains (Fig. 4c). This localized

156 shear surface is underlain by a zone of randomly oriented, inequigranular, irregular graphite grains (Fig. 4d). In places, most

157 of the graphite grains are aligned with their basal (001) planes parallel to the slip direction, and form compacted layers,

158 defining a weak fabric development (Fig. 4e). There has been some dilation along these cleavage planes, and the spaces thus

159 created are filled with smaller graphite grains with their (001) planes sub-perpendicular to the shear direction (Fig. 4e).

160 Locally, intensely fractured grains are also observed (Fig. 4f).

161 **4 Discussion**

162 **4.1 Mechanical behavior**

163 Graphite in our experiments shows mechanical behavior consistent with other mechanical studies of pure graphite gouges.

164 Our results display low μ_{ss} values (from ~0.1 to ~0.2; Table 1) as did the low-pressure deformation experiments of

165 carbonaceous material performed by Morrow et al. (2000), Moore & Lockner (2004), Oohashi et al. (2011, 2013), Kuo et al.

166   (2014), and Rutter et al. (2016). The low frictional strength of graphite is well known and has been attributed to its sheet

167   structure composed of covalently bonded carbon atoms held together only by van der Waals forces. These weak interlayer

168   bonds along (001) planes are easily broken during shear (Moore & Lockner, 2004; Rutter, et al., 2016). Initial μ_{peak} followed

169   by strain weakening during deformation experiments of graphite gouges has been previously explained with the work

170   involved in rotating the grains with their (001) planes sub-parallel to the shear surfaces, which puts them in the optimal

171   position for shearing along the weak interlayer bonds (Morrow et al., 2000; Moore & Lockner, 2004; Rutter, et al., 2016).

172   Controversially, Oohashi et al. (2011) reported an absence of μ_{peak} in pure graphite gouges sheared at ≤ 2 MPa with sliding

173   velocities of 1.3 m/s. Instead shearing started and continued at a similar μ throughout their experiments. Our data indicate

174   that μ_{peak} tends to increase with decreasing normal stresses (see experiments at 25 MPa vs. 5 MPa: Fig. 1a; Table 1),

175   therefore, we attribute the discrepancies in graphite frictional strength to the effect of sliding velocity on graphite friction.

176   We hypothesize that higher velocities result in more efficient reorientation of graphite grains, and therefore, μ_{peak} is not

177   present in experiments carried out at seismic rates. This hypothesis is also consistent with the observations from our

178   experiments at 25 MPa that clearly indicate a trend of decreasing μ_{peak} with increasing sliding velocity (Fig. 1a, b; Table 1).

179   We also acknowledge that the imposed velocities in the experiments by Oohashi et al. (2011) were substantially different to

180   ours, and shearing at those seismic rates may cause partial frictional heating. Therefore, graphite frictional strength in their

181   experiments may be related to thermally-activated weakening mechanisms (Nakatani, 2001) that are only significant at these

182   high velocities.

183   We also observed shear strain variations in the various samples (Fig. 1b, c and d) that are systematically related to the

184   conditions of the experiments. The calculated shear strain (or the ratio of shear displacement to measured layer thickness) is

185   linearly dependent on the applied normal stress, and shear strains are significantly higher in the experiments performed at 25

186   MPa than the ones at 5 MPa due to better compaction and thinning of the sheared graphite gouges. Furthermore, slip rates

187   also play a role in the accommodated total shear strain, and shear strain increases with increase in the applied sliding

188   velocities but only in the high-pressure experiments (Fig. 1b). As we previously suggested, higher velocities may result in

189   more efficient reorganization of graphite grains, and thus further progressive thinning of the graphite gouges occurred.

190   However, we cannot explain the absence of similar trend at the 5 MPa experiments by our results. There are too few of these

191   relationships to fully characterize the effect of sliding velocity on shear strain accumulation in graphite gouges, and more

192   mechanical data of this sort need to be collected in future.

193   **4.2 Structural disorder of graphite**

194   Our experimental study clearly demonstrates transformation of fully/highly crystalline graphite (with R2 ratios ranging from

195   0 to 0.327; Fig. 2; S1) into comparatively poorly organized graphitic carbon (with R2 ratios up to 0.661; Fig. 2; S1), which

196   indicates significant graphite disorder with increasing strain at the tested aseismic sliding velocities (Fig. 3). We also

197   acknowledge that the slickenlined surfaces that were produced experimentally contain some graphite that yield spectra

198   comparable to those acquired from the starting material i.e. there is highly crystalline graphite that appears as unaffected by

199   the deformation. However, at least some of these spectra are derived from undeformed graphite powder that underlies the

200   shear surfaces and could not be entirely removed during sample preparation due to the fragile nature of the samples. It is also

201   possible that some non-deformed graphite powder was accidently measured through the fractures that are cross-cutting the

202   accumulated shear surfaces (Fig. 4a). But even if some graphite did not undergo mechanical modification during the

203   experiments, the results overall validate that structural disorder of graphite can result from shear deformation subsequent to

204   the graphitization process.

205   Our findings contradict the paradigm that the degree of graphite crystallinity is determined by an irreversible maturation of

206   carbonaceous material (Beyssac et al., 2002a; Bonijoly et al., 1982; Buseck and Beyssac, 2014; Wopenka and Pasteris,

207   1993). Therefore, graphite should not be considered as a stable mineral, especially in active tectonic settings, where

208   mechanical motions, such as fault creep, may cause disordering of the structure of carbonaceous material that formed during

209   typical graphitization processes. Similar assumptions have been made on graphite in intensely deformed cataclasites

210   (comprising crushed mylonitic chips floating in a fine-grained matrix) that is significantly disordered in comparison with

211   graphite in the spatially associated mylonitic rocks (Kirilova et al, in review; Nakamura et al., 2015).

212   We have experimentally proven that shear strain can not only affect the final structural order of graphite but also manifests

213   as a controlling parameter in the transformation process (Fig. 3; Table 2). Previous authors have suspected that shear strain

214   may play an important role for graphite modifications, and evidence for this has been found in graphite crystallinity

215   variations in natural samples from active fault zones (Kirilova et al, in review; Nakamura et al., 2015), and strained rocks in

216   metamorphic terrains (Barzoi, 2015; Large et al., 1994). Thus, we conclude that the previously proposed model of

217   progressive graphitization due to increase of temperature (Bonijoly et al., 1982) does not completely reflect the graphite

218   formation mechanisms.

219   Furthermore, graphite can form or be transported at various depths by tectonic processes, and therefore, it can be exposed to

220   different lithostatic pressures. We demonstrated that during shearing higher normal stress results in an increase of shear

221   strain (Fig. 1b), and thus causes a higher degree of graphite disorder (Fig. 3; Table 2). This outlines the significant effect of

222   lithostatic pressure on graphite crystallinity that has been undervalued until now (Bonijoly et al., 1982; Wopenka and

223   Pasteris, 1993; Bustin et al, 1995; Beyssac et al. 2002b). Previous experimental studies have identified initiation and

224   enhancement of graphitization under pressure (i. e. increase in graphite crystallinity) but only at nanometer scale (Bonijoly et

225   al., 1982; Beyssac et al., 2003). Nevertheless, we speculate pressure should be also considered as a factor that can determine

226   the degree of graphite crystallinity during both graphitization and graphite structural modifications.

We have investigated the effects of shear strain and pressure on graphite crystallinity during shear deformation with aseismic velocities, using a starting material with uniform properties (i.e. highly crystalline graphite powder). In contrast, Kuo et al. (2014) and Oohashi et al. (2011) simulated fault motions in synthetic and natural carbonaceous material with variable degree of maturity at the start of the experiments (ranging from amorphous carbonaceous material to crystalline graphite). Both studies reported graphitization of carbonaceous material due to localized frictional heating rather than structural disordering. These experiments reveal the impact of seismic velocities on graphite structural order and the fact their findings differ so markedly from ours highlights the complexity of graphite transformations in fault zones.

Our microstructural observations provide some indications of the deformation processes that affected graphite structural order. They reveal a thin slip-localized zone (Fig. 4d), underlined by a less deformed zone with typical cataclastic fabric (random fabric (Fig. 4d), affected by occasional fractures (Fig. 4f)). These observations demonstrate that brittle processes operated during shearing and we infer these processes resulted in the structural disorder of graphite, manifested as changes in the Raman spectra. However, crustal fault zones do not only accommodate brittle deformation; at `higher temperatures, confining pressures, and lower strain rates, localised shearing may be accommodated by plastic mechanisms (White et al., 1980). We hypothesize that graphite crystallinity can also be influenced by plastic deformation as also suggested in previous studies by Large et al. (1994), Bustin et al. (1995), Barzoi et al. (2015). Investigating this hypothesis and identifying the exact effects of strain on graphite crystallinity during ductile deformation remain goals for future research.

4.3 Implications for graphite thermometry

The crystallographic structure of graphite measured by Raman spectroscopy has been applied as a thermometer that relies on progressive maturation of originally-organic carbonaceous material during diagenesis and metamorphism. Previous studies have focused on calibrating this thermometer. The current best calibration is described by the following equation T (ºC) = -445 * R2 + 641 ± 50 (Beyssac et al. 2002) by inferring a linear correlation between R2 ratio and peak metamorphic temperatures. However, this thermometer disregards the effects of mechanical modifications of the graphite structure, which this study has identified as having a substantial influence on graphite crystallinity in deformed rocks at sub-seismic velocities.

Our experiments demonstrate a shear strain-dependent increase of the R2 ratio of initially highly crystalline graphite powder due to shear deformation (Fig. 3; Table 2). In natural analogues, the pre-shear graphite would yield temperatures up to 641 ± 50 ºC (S1), which is the upper limit of the calibrated thermometer (Beyssac et al. 2002). Whereas, the sheared samples would indicate peak metamorphic temperatures as low as 347 ± 50 ºC (estimated from the most strained samples; S1). Thus, we experimentally prove that in active tectonic settings graphite thermometers may underestimate the peak metamorphic temperatures by < 300 ºC. In cataclasites from the Alpine Fault zone, New Zealand (Kirilova et al., in review) and fault zones of the Hidaka metamorphic belt, Japan (Nakamura, et al., 2015), the graphite thermometer yields temperature

258 discrepancies of more than 100 ℃ compared to temperature estimates derived both from the surrounding high-grade

259 amphibolite facies mylonites and the lower grade equilibrium cataclastic phases (marked by chlorite alteration). Barzoi

260 (2015) also described differences of ~ 150 ℃ in graphite temperatures between strained and less strained low grade

261 metamorphic rocks from Parang Mountains, South Carpathians.

262 We conclude that shear strain calibration of the current graphite thermometer is needed and we propose an appropriate

263 adjustment based on our dataset. Fig. 3 illustrates good correlation between the average R2 and the shear strain measured

264 within a sample, which can be described by the following equation (1):

265 $y = 495.9 * \gamma^{4.875} + 1.117$ with a correlation coefficient $R^2 = 0.96$ (1)

266 where γ = shear strain.

267 However, a calibration of the existing graphite thermometer could be still insufficient to permit reliable temperature

268 estimates in active tectonic settings because of the variable slip rates likely to be encountered in fault zones.

269 **5 Conclusions**

270 We have experimentally demonstrated that graphite crystallinity is not irreversible by performing shear deformation

271 experiments at aseismic sliding velocities on graphite gouges composed of powdered highly-organized graphite. Our results

272 clearly demonstrate significant decrease in graphite structural order, which is a function of the total shear strain attained

273 during the various experiments. We also observed a trend of increasing shear strain within a sample with increase in the

274 applied normal stresses and sliding velocities. This reveals the complexity of graphite structural modifications and highlights

275 the significance of the various parameters that can affect the graphitization process. Furthermore, our findings compromise

276 the validity of the calibrated graphite thermometers as they may underestimate the peak metamorphic temperatures in active

277 tectonic settings. Thus, we tentatively suggest a shear strain calibration of these thermometers.

278 **Acknowledgments**

Solid Earth
Discussions

Open Access

EGU

References

Barzoi, S. C.: Shear stress in the graphitization of carbonaceous matter during the low-grade metamorphism from the northern Parang Mountains (South Carpathians)—Implications to graphite geothermometry, International Journal of Coal Geology, 146, 179-187, 2015.

Beyssac, O., Goffé, B., Chopin, C. and Rouzaud, J. N.: Raman spectra of carbonaceous material in metasediments: a new geothermometer, Journal of metamorphic Geology 20.9: 859-871, 2002a

Beyssac, O., Rouzaud, J. N., Goffé, B., Brunet, F., and Chopin, C.: Graphitization in a high-pressure, low-temperature metamorphic gradient: a Raman microspectroscopy and HRTEM study. Contributions to Mineralogy and Petrology, 143(1), 19-31, 2002b

Beyssac, O., Brunet, F., Petitet, J. P., Goffé, B., and Rouzand, J. N.: Experimental study of the microtextural and structural transformations of carbonaceous materials under pressure and temperature. European Journal of Mineralogy, 15(6), 937-951, 2003.

Bonijoly, M., Oberlin, M. and Oberlin, A.: A possible mechanism for natural graphite formation. International Journal of Coal Geology 1.4: 283-312, 1982.

Buseck, P. R. and Beyssac, O.: From organic matter to graphite: Graphitization, Elements 10.6: 421-426, 2014.

Bustin, R. M., Ross, J. V., and Rouzaud, J. N.: Mechanisms of graphite formation from kerogen: experimental evidence, International Journal of Coal Geology, 28(1), 1-36, 1995.

Collettini, C., Di Stefano, G., Carpenter, B., Scarlato, P., Tesei, T., Mollo, S., Trippetta, F., Marone, C., Romeo, G. and Chiaraluce, L.: A novel and versatile apparatus for brittle rock deformation, International journal of rock mechanics and mining sciences, 66, 114-123, 2014.

Crespo, E., Luque, F. J., Barrenechea, J. F., and Rodas, M.: Influence of grinding on graphite crystallinity from experimental and natural data: implications for graphite thermometry and sample preparation, Mineralogical magazine, 70(6), 697-707, 2006.

Kirilova, M., Toy, V., Timms, N., Little, T., Halfpenny, A., Menzies. C., Craw, D., DFDP-1 Science Team, and DFDP-2 Science Team: Transformation of graphite by tectonic and hydrothermal processes in an active plate boundary fault zone, Alpine Fault, New Zealand, in review.

312   Kuo, L. W., Li, H., Smith, S. A., Di Toro, G., Suppe, J., Song, S. R., and Si, J.: Gouge graphitization and dynamic fault

313   weakening during the 2008 Mw 7.9 Wenchuan earthquake. Geology, 42(1), 47-50, 2014.

314   Large, D. J., Christy, A. G., and Fallick, A. E.: Poorly crystalline carbonaceous matter in high grade metasediments:

315   implications for graphitisation and metamorphic fluid compositions, Contributions to Mineralogy and Petrology, 116(1-2),

316   108-116, 1994.

317   Manatschal, G.: Fluid-and reaction-assisted low-angle normal faulting: evidence from rift-related brittle fault rocks in the

318   Alps (Err Nappe, eastern Switzerland), Journal of structural geology, 21(7), 777-793, 1999.

319   Moore, D. E., and Lockner, D. A.: Crystallographic controls on the frictional behavior of dry and water-saturated sheet

320   structure minerals, Journal of Geophysical Research: Solid Earth, 109(B3), 2004.

321   Morrow, C. A., Moore, D. E., and Lockner, D. A.: The effect of mineral bond strength and adsorbed water on fault gouge

322   frictional strength, Geophysical research letters, 27(6), 815-818, 2000.

323   Nakamura, Y., Oohashi, K., Toyoshima, T., Satish-Kumar, M., and Akai, J.: Strain-induced amorphization of graphite in

324   fault zones of the Hidaka metamorphic belt, Hokkaido, Japan, Journal of Structural Geology 72: 142 – 161, 2015.

325   Nakatani, M.: Conceptual and physical clarification of rate and state friction: Frictional sliding as a thermally activated

326   rheology, Journal of Geophysical Research: Solid Earth, 106(B7), 13347-13380, 2001.

327   Oohashi, K., Hiros, T. and Shimamoto, T.: Shear-induced graphitization of carbonaceous materials during seismic fault

328   motion: experiments and possible implications for fault mechanics, Journal of Structural Geology 33.6: 1122-1134, 2011.

329   Oohashi, K., Hirose, T. and Shimamoto, T.: The occurrence of graphite-bearing fault rocks in the Atotsugawa fault system,

330   Japan: origins and implications for fault creep, Journal of Structural Geology 38: 39-50, 2012.

331   Rietmeijer, F. J., and Mackinnon, I. D.: Poorly graphitized carbon as a new cosmothermometer for primitive extraterrestrial

332   materials. Nature, 315(6022), 733-736, 1985.

333   Savage, R. H.: Graphite lubrication, Journal of Applied Physics 19.1: 1-10, 1948.

334   Toy, V.G., Niemeijer, A.R., Renard, F. Wirth, R., and Morales, L.: Striation and slickenline development on quartz fault

335   surfaces at crustal conditions: origin and effect on friction. Journal of Geophysical Research, doi: 10.1002/2016JB013498, in

336   press.

White, S. H., Burrows, S. E., Carreras, J., Shaw, N. D., & Humphreys, F. J.: On mylonites in ductile shear zones, Journal of Structural Geology, 2(1-2), 175-187, 1980.

Wopenka, B., and Pasteris, J. D.: Structural characterization of kerogens to granulite-facies graphite: applicability of Raman microprobe spectroscopy, The American Mineralogist, 78(5-6), 533-557, 1993.

Zulauf, G., Kleinschmidt, G., and Oncken, O.: Brittle deformation and graphitic cataclasites in the pilot research well KTB-VB (Oberpfalz, FRG), Geological Society, London, Special Publications, 54(1), 97-103, 1990.

Table 1. Summary of the conditions at which experiments were carried out and results.

Table 2. Summary of the relationship between shear strain and average R2 within a sample. The conditions of each experiment are also given as follows: applied normal stress in MPa, slip rates in μm/s and sliding displacement in mm.

Figure 1. Plots of mechanical data (a) friction coefficient, μ vs. displacement (b), (c), (d) friction coefficient, μ vs. shear strain.

Figure 2. Representative Raman spectra illustrating: (i) the most crystalline graphite (left column) within a sample; (ii) graphite with approximate average crystallinity per sample (middle column); and (iii) the most disordered graphite (right column) encountered in each sample. The R2 ratio for each spectrum is also noted in italic font.

Figure 3. Plot of the average R2 ratio vs shear strain accumulated during each experiment.

Figure 4. SEM images, obtained from the deformed graphite gouge during experiment 8 (normal stress at 25 MPa with 1 μm/s sliding velocity), show: (a) Slickenlines ornamenting the shear surface; (b), (c) A well-compacted layer of aligned graphite grains, which make up the shear surface. Bright patches due to a differential charging effect; (d) A less deformed zone with typical cataclastic fabric, underlying the shear surface; (e) Dilated cleavage planes in large graphite grains filled with smaller platy graphite grains oriented sub-perpendicular to the shear direction; (f) Fractured graphite grains.

Supplementary material 1 (S1). Raman data from 20 spectra per sample together with calculated R2 ratio and average R2 value for each sample. The last column represents temperature estimated by the current best calibration of a Raman-based thermometer: $T (°C) = - 445 * R2 + 641 \pm 50$.

Experiment number	Normal stress (MPa)	Sliding velocity (µm/s)	Displacement (mm)	Peak friction (μ_{peak})	Steady state friction (μ_{ss})	Shear strain maximum (γ)
1	5	1	20	0.53	*0.22*	17.70
2	5	1	10	0.53	0.22	8.17
3	5	1	5	0.52	*not reached*	4.23
4	5	10	20	0.53	0.24	20.45
5	5	100	20	0.57	0.22	16.89
6	5	100	10	0.55	0.22	9.80
7	5	100	5	0.57	*not reached*	3.87
8	25	1	20	0.43	0.17	21.45
9	25	10	20	0.43	0.17	31.86
10	25	100	20	0.41	0.14	46.77

362

363   **Table 1.** Summary of the conditions at which experiments were carried out and results.

364

365

366

367

368

369

370

371

372

373

374

375

376

Sample	Experimental conditions	Shear strain (γ)	Average R2
Pre-shear graphite	N/A	N/A	0.173
Exp. 2	5 MPa, 1 μm/s, 10 mm	8.17	0.438
Exp. 6	5 MPa, 100 μm/s, 10 mm	9.80	0.430
Exp. 5	5 MPa, 100 μm/s, 20 mm	16.89	0.454
Exp. 1	5 MPa, 1μm/s, 20 mm	17.70	0.506
Exp. 4	5 MPa, 10 μm/s, 20 mm	20.45	0.517
Exp. 8	25 MPa, 1 μm/s, 20 mm	21.45	0.520
Exp. 9	25 MPa, 10 μm/s, 20 mm	31.86	0.580
Exp. 10	25 MPa, 100 μm/s, 20 mm	46.77	0.604

377 **Table 2.** Summary of the relationship between shear strain and average R2 within a sample. The conditions of each
378 experiment are also given as follows: applied normal stress in MPa, slip rates in μm/s and sliding displacement in mm.

379

380

381

382

383

384

385

386
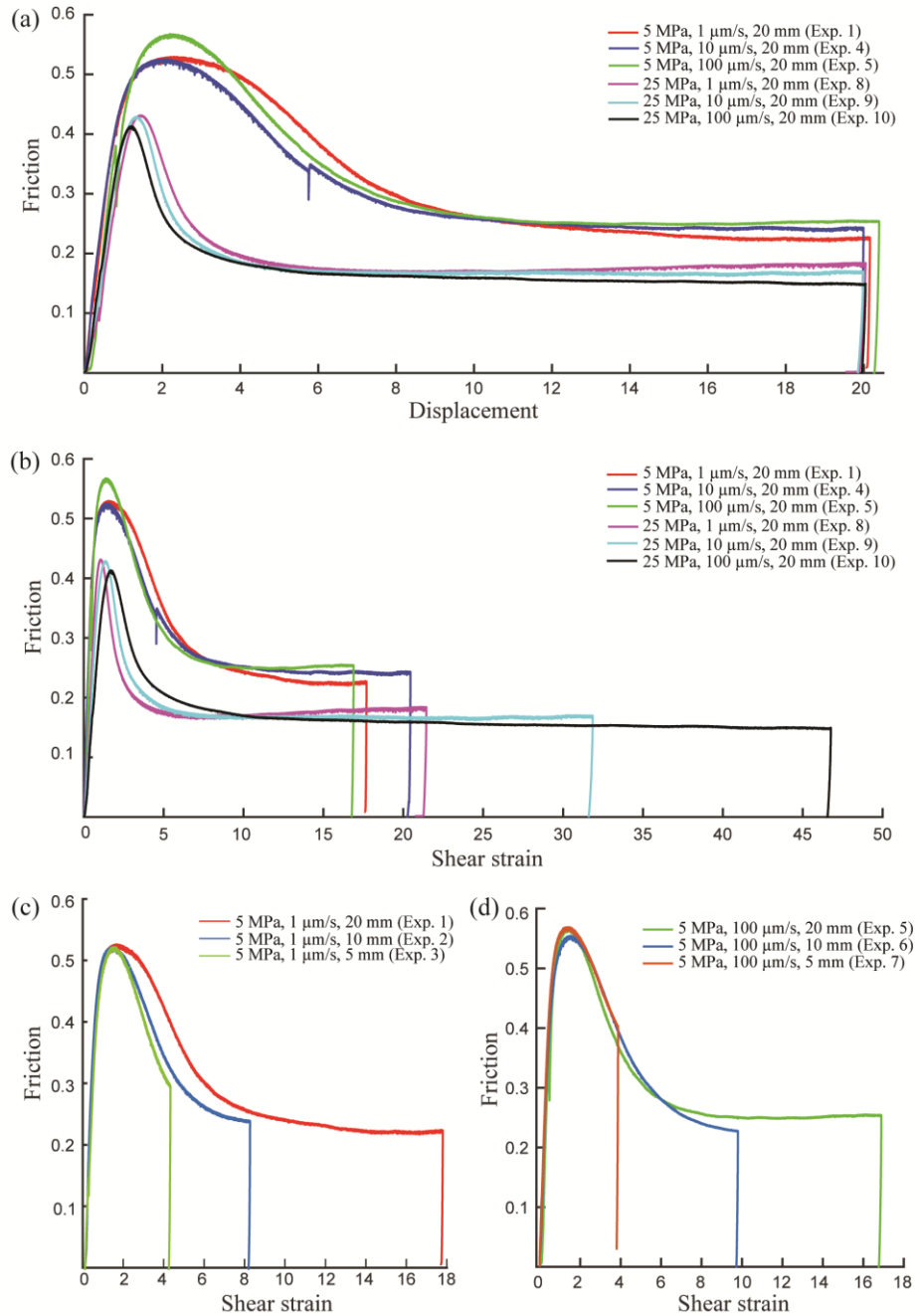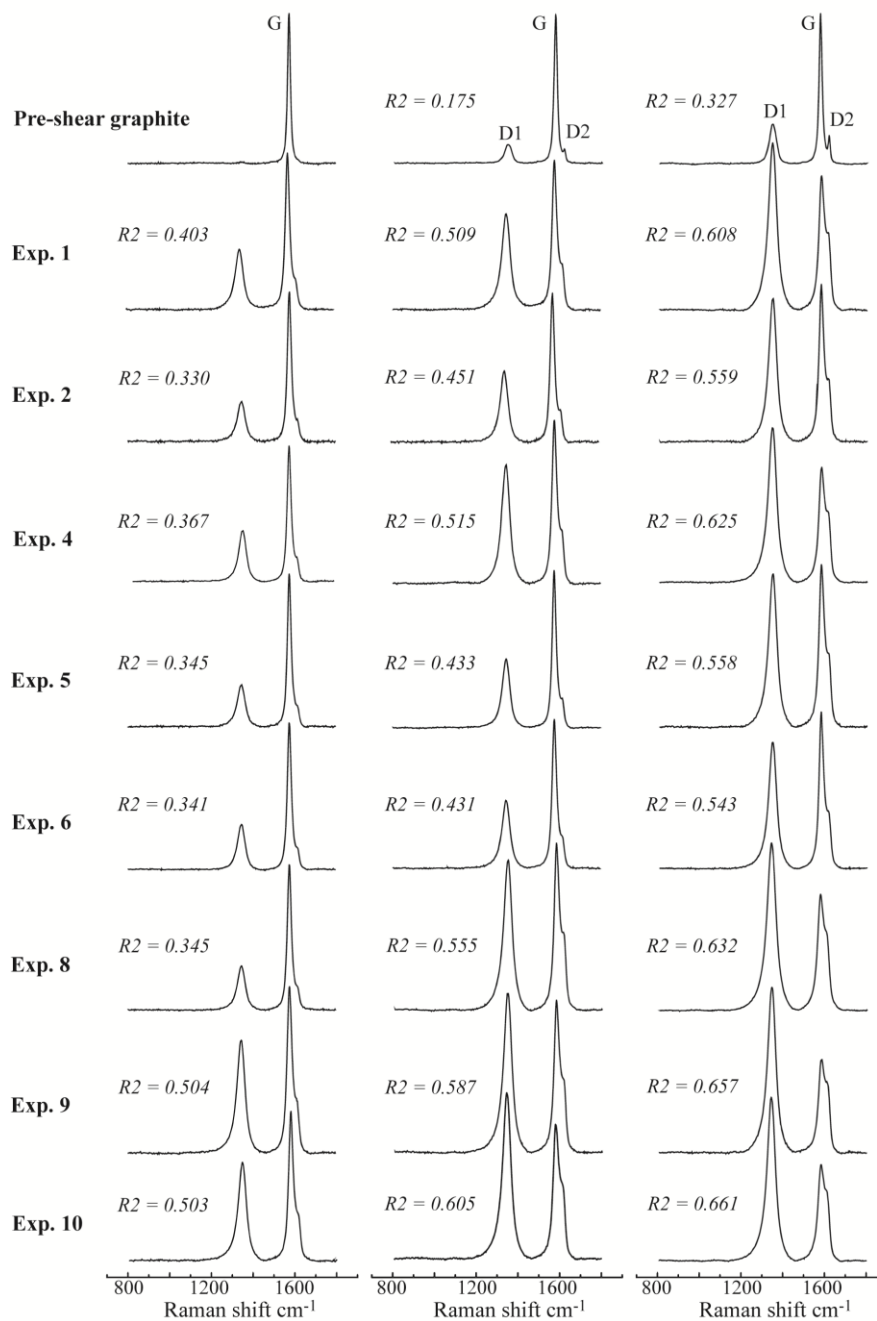
387

388

389

Figure 1. Plots of mechanical data (a) friction coefficient, μ vs. displacement (b), (c), (d) friction coefficient, μ vs. shear strain.
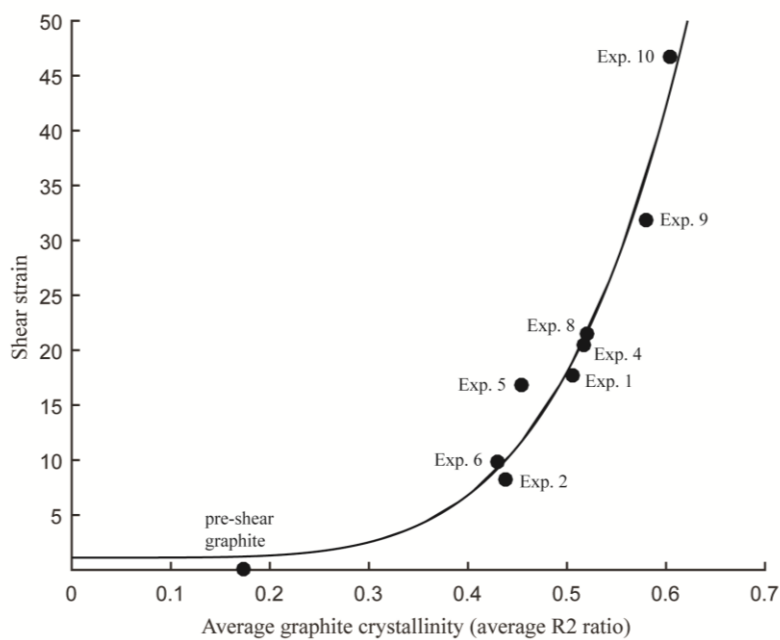
Figure 2. Representative Raman spectra illustrating: (i) the most crystalline graphite (left column) within a sample; (ii) graphite with approximate average crystallinity per sample (middle column); and (iii) the most disordered graphite (right column) encountered in each sample. The R2 ratio for each spectrum is also noted in italic font.

398

399

Figure 3. Plot of the average R2 ratio vs shear strain accumulated during each experiment.

401

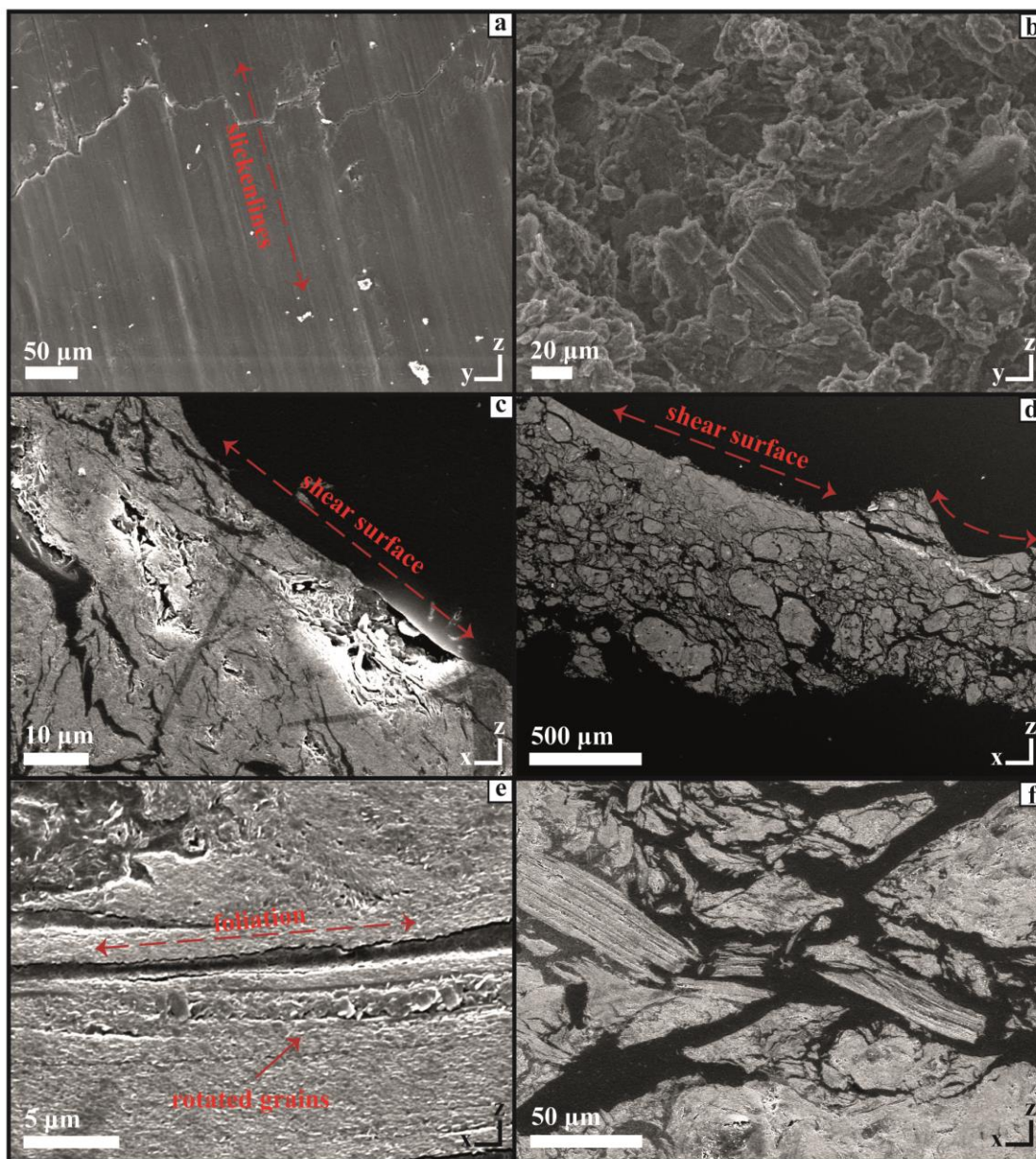402

403

404

405

406

407

Solid Earth

Open Access

EGU

Discussions

408

Figure 4. SEM images, obtained from the deformed graphite gouge during experiment 8 (normal stress at 25 MPa with 1

µm/s sliding velocity), show: (a) Slickenlines ornamenting the shear surface; (b), (c) A well-compacted layer of aligned

graphite grains, which make up the shear surface. Bright patches due to a differential charging effect; (d) A less deformed

zone with typical cataclastic fabric, underlying the shear surface; (e) Dilated cleavage planes in large graphite grains filled

with smaller platy graphite grains oriented sub-perpendicular to the shear direction; (f) Fractured graphite grains.